Numerical study on performance enhancement of a solid oxide fuel cell using gas flow field with obstacles and metal foam

Results in Engineering 23 (2024) 102457

Contents lists available at ScienceDirect

Results in Engineering

journal homepage: www.sciencedirect.com/journal/results-in-engineering

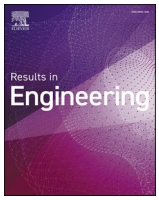

Numerical study on performance enhancement of a solid oxide fuel cell using gas flow field with obstacles and metal foam

Asma Naouar [a], Domenico Ferrero [b,*], Massimo Santarelli [b], Hacen Dhahri [a], Abdallah Mhimid [a]

[a] University of Monastir, National Engineering School of Monastir, Street Ibn Eljazzar, 5019, Monastir, Tunisia
[b] Department of Energy (DENERG), Politecnico di Torino, Corso Duca degli Abruzzi, 24, 10129, Turin, Italy

ARTICLE INFO

Keywords:
Solid oxide fuel cell
CFD simulation
Obstacles
Metal foam
Current density distribution

ABSTRACT

This study investigates the impact of gas flow field design on the performance of a solid oxide fuel cell (SOFC). A three-dimensional numerical model of the cell and channel is developed to simulate the use of metal foam as flow distributor, along with the presence of obstacles in the gas flow channels. The model is calibrated using experimental data and applied to simulate four relevant cases combining metal foam and obstacles, compared to a straight channel structure. The results demonstrate the positive impact of flow-field modifications on the distribution of species along the cell's active layers. It is found that, even though the pressure drops are affected, reactant gases are more uniformly distributed across the active electrode of the cell, reducing mass transport losses and enhancing current density. Simulations performed at a cell voltage of 0.7 V indicate that incorporating a metal foam as flow distributor increases the maximum current density by 26 % compared to the conventional straight flow design. Furthermore, combining metal foam with obstacles results in the best performance, achieving a 34 % increase in the maximum current density.

1. Introduction

A fuel cell is a power generator that converts the chemical energy of fuels into electrical energy and heat. Nowadays, fuel cells have garnered significant attention due to their numerous benefits, which include their electrical performance, cleaner energy production, and compactness [1–5]. Among these, the solid oxide fuel cell (SOFC) stands out as it operates at high and intermediate temperatures (600 °C–800 °C), allowing for the utilization of both hydrocarbons and hydrogen fuels [6–12]. The SOFC is regarded as one of the most promising candidates for power production thanks to its fast electrochemical reaction, high efficiency, and especially, fuel flexibility [13–16].

Several studies have explored different flow distribution strategies to ensure homogeneous distribution of reactants in fuel cells. Saied et al. [17] simulated different types of flow channels, including traditional parallel, helical, multiple-entry serpentine, and triple-entry serpentine channels, to achieve a homogenous reactant distribution. Bhattacharya et al. [18] observed that serpentine channels led to increased fuel consumption and more uniformly distributed current compared to straight channel designs. Duhn et al. [19] elaborated a gas flow distribution using parallel channels, and deduced that the ideal flow homogeneity index would be 0.978. Other studies have combined newly designed features with traditional designs [20,21]. Additionally, other researchers have focused on optimizing interconnect parameters. Moreno-Blanco et al. [22] studied the impact of the channel-electrode interface area on the performance of the cell, finding its peak when the channel-electrode interface area ratio was 0.36. Manglik et al. [23] analyzed mass and heat transfer in SOFCs with various geometries of interconnect ducts (triangular, trapezoidal and rectangular). Rectangular-shaped channels were found to offer uniform temperature distribution and higher performance compared to triangular and trapezoidal shapes, consistent with findings by Khazee et al. [24]. Huang et al. [25] investigated the flow homogeneity in various types of interconnectors and its effect on the efficiency of the SOFC.

Several studies proposed enhanced flow field designs to attain better uniformity of flow distribution and current [19,26–30]. Furthermore, many researchers have inserted different obstacles in the flow channel to optimize their geometry and improve fuel cell performance [31,32]. The flow pattern can be regulated by placing obstacles (in terms of number and shape) in electrode channels. For example, Chellehbari et al. [33] investigated the effect of placing rectangular, triangular, and trapezoidal obstacles in the flow channels on the performance of the cell.

* Corresponding author.
E-mail address: domenico.ferrero@polito.it (D. Ferrero).

https://doi.org/10.1016/j.rineng.2024.102457
Received 17 December 2023; Received in revised form 14 June 2024; Accepted 20 June 2024
Available online 22 June 2024

They found that applying seven triangles raised the average current density by 15 % compared to the base case (flow channel without obstacles), and the power of the SOFC increased by 35 %. Bilgili et al. [34] demonstrated that the presence of obstacles within the electrode channels enhanced the concentration distribution throughout the channels and the propagation of gaseous reactants via the gas diffusion layer (GDL); consequently, the electrochemical reactions were boosted. Forty-nine different configurations were compared to demonstrate the quantitative impact of parameters on the functionality of the baffled flow field [35].

Several researchers have realized that the shape, size, arrangement and number of obstacles have a significant effect on fuel cell performance [36–39]. While the presence of baffles in the channels can enhance the performance of the fuel cell, it also increases pressure drops and uneven gas distribution in the catalyst layer, and the presence of numerous baffles makes this more noticeable. To address the challenges associated with flow channels in fuel cells, one potential solution is to substitute the flow channels with a porous medium, such as metal foam. Metal foam offers high porosity, flexible permeability, and lightweight properties, making it an effective flow distributor [40]. Various experimental and numerical studies of metal foam applications have been published in the literature. Metal foam flow fields have been widely applied in PEMFCs, and thorough studies have shown that they can greatly improve cell performance [41–47]. Kumar et al. [48] suggested that using metal foam could minimize the size and weight of fuel cells, while Afshari et al. [49] demonstrated that using metal foam as a flow field provides more uniform temperature distribution, and that increasing its porosity enhances cell performance. In addition, it was demonstrated that the permeability of metal foam has a considerable impact on fuel cell efficiency [50,51], and proper foam permeability should be chosen for optimum pressure drop [52]. The experimental results of Tsai et al. [53] demonstrated that metal foam promotes the uniform distribution of gas reactants in the catalyst layers. Moreover, SOFC operating conditions have been adapted to several porous metal materials [54,55]. Zielke et al. [56] experimentally investigated the degradation of cell performance using a Cu–Mn foam as cathode contact material. Cu–Mn foam was discovered to be suitable for extended operation and appropriate as an SOFC cathode distributor. To ensure that SOFC flows were distributed uniformly and current was collected, Iwai et al. [57] simulated cell operation using a porous material as a flow distributor. Zhan et al. [58] simulated a cell using metal foam to replace the cathode flow field, which led to an enhancement of the output power by 13.74 % compared to a conventional channel. In fact, the oxygen concentration, electron transport, and temperature of the SOFC were more uniformly distributed.

However, the impacts of porous material distributors on SOFCs are poorly represented in few numerical simulations. Addressing this research gap, our study aims to explore different patterns that result in improved reactant distribution. In this study, a three-dimensional numerical model of an anode supported SOFC is developed to investigate the impact of inserting obstacles inside the flow channels and utilizing a metal foam instead of conventional flow channels on fuel cell performance. The model is calibrated using experimental data and applied to simulate four relevant cases that combine different SRU (single repeating unit) designs with and without channels, metal foam and obstacles. The improvement of the performance is analyzed in terms of the increase of cell current density at fixed voltage (i.e. increased power density).

The numerical analysis of the design of the flow-field is the first step in the process of maximizing the performance fuel cell technology, ultimately reducing the cost of electricity production. This process involves validating the energy analysis of the improved design at SRU-prototype level through experimental and uncertainty analysis, as reported in relevant literature for both low- and high-temperature fuel cells [59–64]. Following this, a cost analysis of the stack design must be performed to assess the impact of the changes on the investment cost of the fuel cell. In the case of improving the SOFC's flow-field, the design changes minimally affect the manufacturing of the interconnect. Moreover, adding a metal mesh (typically Nickel for the anode) – if not already present in the stack – does not significantly alter the type or amount of materials used in the stack. Therefore, the design improvement is expected to have a negligible impact on the stack cost, likely keeping it within the range reported for state-of-the-art SOFC stacks [65,66]. The final step in determining the cost of the produced electricity is the techno-economic analysis (TEA). The TEA considers the use-case of the stack, taking into account its operation profile and the cost of the fuel. For example, using green hydrogen as fuel significantly impacts the final electricity cost, which varies with the specific electrolysis technology and renewable sources employed [67–70]. Another example is using SOFCs for co-generation, typically fueled by natural gas or biogas [71].

Given that the cost of the electricity produced by a SOFC is primarily influenced by the materials and manufacturing costs of the stack – which are not expected to change significantly with the design modification – and external factors like fuel cost, performance improvement is the key determinant factor of the success of a design improvement. For this reason, the present work focuses on the numerical analysis of SOFC performance improvements, with experimental validation to be addressed in future studies.

2. Numerical model

2.1. Geometry

The three-dimensional numerical model of a hydrogen-fueled SOFC unit has been developed.

Fig. 1 shows the schematic of the simulated fuel cell unit, consisting of active cathode and anode layers (AFL/CFL), supporting anode layer (ASL), cathode diffusion layer (CDL), electrolyte and interconnectors, dividing the total cell into seven zones. The material is Ni for ASL, Ni-8YSZ for AFL, dense 8YSZ for electrolyte, LSM for CDL, and LSM-8YSZ composite for CFL [72]. The model has been developed and implemented in the commercial software COMSOL Multiphysics (version 5.3). The geometry parameters are shown in Table 1.

The assumptions applied are the following: the SOFC operates at steady-state conditions, flow conditions are established laminar and incompressible in the channels, the involved gases in both channels are assumed to behave as ideal gases, the ionic and electronic conductors are considered to be isotropic and homogenous, gas leakage and radiation heat transfers are neglected.

The equation for momentum, mass, electron, ion, and heat transport have been simultaneously solved, as described in the following section.

2.2. Governing equations

Two basic reactions occurring in the anode and cathode are considered, as the cell has been simulated in the operation with humidified hydrogen at the anode and air at the cathode.

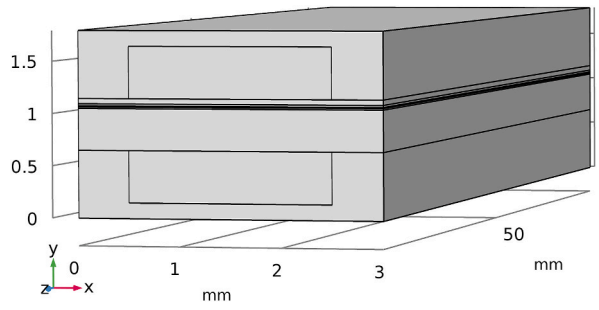

Fig. 1. Schematic of the single-channel SOFC model.

Table 1
Geometry size of the single cell SOFC [72,73].

	Height- y [10^{-6}]/m	Depth-x [10^{-3}]/m
Gas channel	500	2
Interconnects ribs		0.5
Interconnects	650	3
Anode support layer	400	
Anode active layer	15	
Electrolyte	10	
Cathode active layer	20	
Cathode diffusion layer	50	
Obstacle	250	2

At the cathode, oxygen is reduced to ionic form by electrons as follows [20]:

$$\frac{1}{2}O_2 + 2e^- \Leftrightarrow O^{2-} \tag{1}$$

At the anode, hydrogen is adsorbed on the Ni surface at the TPB; the oxygen ion, passing through the electrolyte, reacts with hydrogen at the anode active layer (AFL).

The reaction results in two electrons and steam.

$$H_2 + O^{2-} \Leftrightarrow H_2O + 2e^- \tag{2}$$

And the overall reaction is given by:

$$H_2 + \frac{1}{2}\,O_2 \Leftrightarrow H_2O \tag{3}$$

Ion and electron transport are considered in order to solve charge conservation equation. Ohm's law is employed for charge balances.

2.3. Ionic and electronic transport

The operating cell voltage is the potential difference between the cathode and the anode current collectors. The governing equations for the ion and electron transport are defined as [74]:

$$\begin{cases} \nabla . i_l = i_v \\ i_l = -\sigma_{eff,l}\nabla\varphi_l \end{cases} \tag{4}$$

$$\begin{cases} \nabla . i_s = i_v \\ i_s = -\sigma_{eff,s}\nabla\varphi_s \end{cases} \tag{5}$$

where φ_l and φ_s are the ionic and the electronic potential respectively, i_v is the volumetric current density obtained from the Butler-Volmer equation, i_l and i_s are the charge fluxes for ions and electrons and $\sigma_{eff,l}$ and $\sigma_{eff,s}$ are the effective ion and electron conductivities.

2.4. Electrochemical model

Due to various polarizations and internal resistance, the working voltage (E) drops compared to the open circuit voltage, and it is expressed as [75]:

$$V = E^{ocv} - \eta_{act} - \eta_{ohm} - \eta_{conc} \tag{6}$$

Where E^{ocv} means the open circuit voltage, the activation polarizations η_{act} reflecting the loss caused by the electrochemical reactions at the electrodes are defined as:

$$\eta_{act,a} = \varphi_s - \varphi_l - E_{eq,a} \tag{7}$$

$$\eta_{act,c} = \varphi_s - \varphi_l - E_{eq,c} \tag{8}$$

Ohmic loss (η_{ohm}) occurs because of the resistance to the flow of ions in the electrolyte and the electrical resistance of materials to the flow of electrons:

$$\eta_{ohm} = i\,.\;\; R_{tot} \tag{9}$$

Here R_{tot} is the total internal resistance in the cell. The concentration polarization η_{conc} are calculated by Ref. [76]:

$$\eta_{conc,a} = \frac{R.T}{n_a.F}\;\; ln\left(\frac{P_{H_2O,TPB}\;.P_{H_2,b}}{P_{H_2,TPB}\;.P_{H_2O,b}}\right) \tag{10}$$

$$\eta_{conc,c} = \frac{R.T}{n_c.F}\;\; ln\left(\frac{P_{O_2,b}}{P_{O_2,TPB}}\right) \tag{11}$$

where the index TPB stands for the three-phase boundary, and b for the boundary between the gas channel and the electrode. When an hydrogen-water steam mixture is used as fuel, then the equilibrium potential for cathode and anode is calculated by Nernst equation [72]:

$$E_{eq,H_2} = \frac{R.T}{2.F}\;\; ln\;\; \frac{P_{H_2}}{P_{H_2O}} \tag{12}$$

$$E_{eq,O_2} = E^0_{H_2/O_2} + \frac{R.T}{4.F}\;\; ln\;\; \left(\frac{P_{O_2}}{P_{O_2,ref}}\right)^{\frac{1}{2}} \tag{13}$$

Where the reversible voltage $E^0_{H_2/O_2}$ is defined as [72]:

$$E^0_{H_2/O_2} = 1.253 \;-\; 2.4516\;.\;10^{-4} \times T \tag{14}$$

The current density (i_v) can be obtained through the Butler-Volmer equation:

$$i_v = Ave\;.\;i_0\;\; \left[\exp\left(\frac{n\alpha F\eta_{act}}{RT}\right) - \exp\left(\frac{n(1-\alpha)F\eta_{act}}{RT}\right)\right. \tag{15}$$

Where i_0 is the exchange current density, F is the Faraday constant, α is the charge transfer coefficient, n is the number of electrons transferred per electrochemical reaction and *Ave* is the electrochemical active area of the corresponding electrode.

The exchange current density, i_0 , refers to the rate that reduced and oxidized species transfer electrons with the electrode, and defined as [72]:

$$i_{0,a} = \gamma_a \left(\frac{P_{H_2}}{P_{H_2,ref}}\right)^A \;\; \left(\frac{P_{H_2O}}{P_{H_2O,ref}}\right)^B \exp\left(\frac{-E_a}{RT}\right) \tag{16}$$

$$i_{0,c} = \gamma_c \left(\frac{P_{O_2}}{P_{O_2,ref}}\right)^C \exp\left(\frac{-E_c}{RT}\right) \tag{17}$$

Where γ_a and γ_c are the exponential factor for anode and cathode, E_a and E_c are the activation energy for anode and cathode, $p_{i,ref}$ and p_i are the reference partial pressure and the partial pressure for species i.

2.5. Momentum transfer

The gases flow in the air and fuel channels equation are solved using the Navier-Stokes equation [72]:

$$\nabla . (\rho u) = 0 \tag{18}$$

$$\rho(u.\nabla)u = \nabla\left[-pI + \mu\left(\nabla u + (\nabla u)^T\right) - \frac{2}{3}\,\mu\,(\nabla . u)I\right)\Big] \tag{19}$$

Where u is the velocity vector, ρ is the density, p is the pressure, I is the unit matrix and μ is the dynamic viscosity.

For the governing equation of momentum conservation in porous electrodes and metal foam, the Brinkman equations are used:

$$\nabla . (\rho u) = Q_m \tag{20}$$

$$\frac{1}{\varepsilon}\rho(u.\nabla)u\frac{1}{\varepsilon}=\nabla\left[-pI+\mu\left(\nabla u+(\nabla u)^{T}\right)-\frac{2}{3}\mu\,(\nabla.u)I\right]-\left(\mu K^{-1}+\frac{Q_m}{\varepsilon^2}\right)u \tag{21}$$

Where ε is the porosity, k represents the permeability, and Q_m is the mass source, which is applied in the active layer of electrode:

$$Q_m=\sum_i\frac{\nu_i\,i_v}{n_eF}\,M_i \tag{22}$$

2.6. Mass transfer

Considering a reacting flow involving a mixture, for the species i, the mass transport through gas diffusion and reactive layers in a fuel cell is given by Refs. [72,74–80]:

$$\rho(u.\nabla)\omega_i=-\nabla.j_i+R_i \tag{23}$$

Where ω_i is the mass fraction, R_i is the mass source term, and j_i is the mass flux vector:

$$j_i=-\rho\,\omega_i\sum_j D_{ij}^{eff}d_j \tag{24}$$

In equation (25) D_{ij}^{eff} represents the effective diffusion coefficient of species i and d_j is the diffusional driving force of the species j.

$$D_{ij}^{eff}=\frac{\varepsilon}{\tau}.\left(\frac{D_{ij}.D_{k,ij}}{D_{ij}+D_{k,ij}}\right) \tag{25}$$

$$D_{k,ij}=\frac{2}{3}\,r_e\sqrt{\frac{8.R.T}{\pi.M_{ij}}} \tag{26}$$

$$M_{ij}=\frac{2}{\frac{1}{M_i}+\frac{1}{M_j}} \tag{27}$$

$$D_{ij}=\frac{0.00143.\;T^{1.75}}{p\,M_{ij}^{1/2}\left(v_i^{\frac{1}{3}}+v_i^{\frac{1}{3}}\right)^2} \tag{28}$$

$$d_j=\nabla x_j+\frac{1}{p}\left[(x_j-\omega_j)\nabla_p\right] \tag{29}$$

Where $D_{k,ij}$ is the Knudsen diffusion coefficient, D_{ij} is the binary diffusivity coefficient and r_e is the average pore radius, and x_j is the mole fraction of species j.

2.7. Heat transport

SOFC have the most elevated working temperature, as high as 800 °C, among of all types of fuel cells. In this study, the local thermal equilibrium is used, therefore the temperature T is assumed to be locally the same for both fluid and solid phase.

The governing equation for energy distribution is [72,74–80]:

$$\rho\,C_p u.\nabla T+\nabla.\left(k_{eff}\nabla T\right)=Q_h \tag{30}$$

The effective thermal conductivity in the porous electrodes k_{eff} can be expressed as:

$$k_{eff}=\varepsilon\,k_g+(1-\varepsilon)k_s \tag{31}$$

Where k_s and k_g are the thermal conductivity of solid and gas.

The heat sources because of the activation, the ohmic and the concentration polarization, and the charge of entropy in electrochemical reaction are calculated as:

$$Q_h=i.\left(-\frac{T\,\Delta S_r}{n_e.F}+\eta_{act}+\eta_{conc}\right)+\sum\frac{i^2}{\sigma} \tag{32}$$

Where ΔS_r is the entropy change for reactions (1) and (2). σ denotes the conductivity for specific material [81,81,81]:

$$(\text{anode})\;\sigma_{Ni}=\frac{9.5\times10^7}{T}\exp\left(\frac{-1150}{T}\right) \tag{33}$$

$$(\text{cathode})\;\sigma_{YSZ}=\frac{4.2\times10^7}{T}\exp\left(\frac{-1200}{T}\right) \tag{34}$$

$$(\text{electrolyte})\;\sigma_{LSM}=3.34\times10^3\exp\left(\frac{-10300}{T}\right) \tag{35}$$

The conductivity will affect the electronic and ionic transport path due to the composition and microstructure of porous electrodes. Therefore, the effective conductivity is corrected as:

$$\sigma_{eff,a,s}=\sigma_{Ni}.\frac{V_{Ni,a}}{\tau_{s,a}} \tag{36}$$

$$\sigma_{eff,el,l}=\sigma_{YSZ}.\frac{V_{YSZ,el}}{\tau_{l,el}} \tag{37}$$

$$\sigma_{eff,c,s}=\sigma_{LSM}.\frac{V_{LSM,c}}{\tau_{s,c}} \tag{38}$$

Where V is the volume fraction for ion conductivity and electron conductivity of the solid phase, and τ is the tortuosity factor.

2.8. Solution method and model validation

The governing equations with the appropriate boundary conditions were numerically solved with COMSOL Multiphysics 5.3, using a stationary segregated solver with direct (MUMPS) linear solver system. The system of equations is segregated in 5 steps: 1- velocity distribution and pressure field for anode and cathode, 2- temperature distribution, 3- ion and electron distribution, 4- Mass fraction distribution on the air side (O_2/N_2), 5- Mass fraction distribution on the fuel side (H_2/H_2O).

The physical parameters used in the model are listed in Table 2 and Table 3.

The grid independence was achieved at 192800 meshing elements and the solution tolerance is defined to 0.001 for each segregated group.

2.9. Case study

In the present study, the impacts of incorporating obstacles within flow channels and using metal foam instead of straight flow channels on

Table 2
Material properties [72,76].

Parameter	Value	Units
Anode thermal conductivity	11	W m^{-1} K^{-1}
Cathode thermal conductivity	6	W m^{-1} K^{-1}
Interconnect thermal conductivity	44.5	W m^{-1} K^{-1}
Electrolyte thermal conductivity	2.7	W m^{-1} K^{-1}
Metal foam thermal conductivity	90	W m^{-1} K^{-1}
Anode specific heat	450	J kg^{-1} K^{-1}
Cathode specific heat	430	J kg^{-1} K^{-1}
Interconnect specific heat	475	J kg^{-1} K^{-1}
Electrolyte specific heat	470	J kg^{-1} K^{-1}
Metal foam specific heat	440	J kg^{-1} K^{-1}
AFL/CFL density	3310	kg m^{-3}
ASL density	3030	kg m^{-3}
CDL density	3300	kg m^{-3}
Interconnect density	7850	kg m^{-3}
Electrolyte density	5160	kg m^{-3}

Table 3
Microstructure parameters [58,72].

Layer	ASL	AFL	CDL	CFL	Metal foam
Porosity	0.44	0.3	0.44	0.3	0.9
Tortuosity	10	10	10	10	2.3
Permeability/m^2	1.73×10^{-11}	1.73×10^{-11}	1.73×10^{-11}	1.73×10^{-11}	1×10^{-9}
Electronic phase volume fraction	0.56	0.28	0.56	0.28	–
Ionic phase volume fraction	–	0.42	–	0.42	–

the efficiency of fuel cell are discussed. Four different cases are explored, as indicated in Fig. 2.

Case A. a SOFC unit with two conventional straight channels, as depicted in Fig. 2a.

Case B. Five rectangular obstacles positioned 20 mm apart from one another in the flow channels (Fig. 2b).

Case C. Utilization of a nickel metallic foam with 90 % porosity as flow distributor in the SOFC unit (Fig. 2c).

Case D. Implementation of both 5 obstacles and use of a nickel metallic foam as a flow distributor simultaneously (Fig. 2d).

All the operating conditions and geometric parameters of the SOFC remain consistent in the four models (Fig. 2).

2.10. Boundary conditions

The inlet gases are assumed to follow laminar flow profiles, with a humidified hydrogen mixture inlet (90 % hydrogen and 10 % water) at the anode and an air inlet consisting of oxygen and nitrogen. At the outlets, boundary conditions are imposed as convective flux, where the pressures are set as atmospheric pressure (1 atm). No-slip condition is applied at the walls.

The inlet gas temperature imposed is the operating temperature of the cell (1000 K). Symmetry is characterized at the bottom and the top of the cell walls. Regarding the electrical potential boundary condition, the cell potential on the surface of interconnect in the cathode side is fixed as the cell operating voltage (0.7 V), while the cell potential on the anode side is set to zero.

More detailed operating conditions are stated in Table 4.

Table 4
Operating conditions [72].

Inlet temperature/K	1000
Operating pressure/atm	1
Operating voltage/V	0.7
Fuel velocity inlet m s^{-1}	0.5
Air velocity inlet m s^{-1}	1
Fuel inlet composition x_{H_2}, x_{H_2O}	0.9; 0.1
Air inlet composition x_{O_2}, x_{N_2}	0.21; 0.79

3. Results

3.1. Model validation

In order to demonstrate that the model applied in this study can realistically simulate the performance of SOFC, the current model is developed under the same experimental conditions as those provided by Fu et al. [82]. For the experiments, the fuel and the air inlet flow rates are 16 Nml/(min.cm^2) and 80 Nml/(min.cm^2) respectively at 800 °C for the SOFC stacks with traditional straight channel interconnectors (SCIs). The cell voltage versus current density curve generated through numerical modeling is displayed in Fig. 3 alongside the curve derived from the experimental data. The maximum error in this validation result is less than 5 %, indicating significant agreement between the experimental and simulation data.

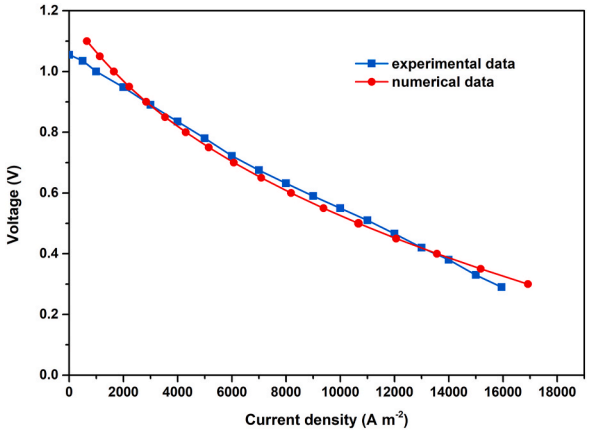

Fig. 3. Comparison of Numerical and experimental polarization curves for the SOFC (Ref. [82]).

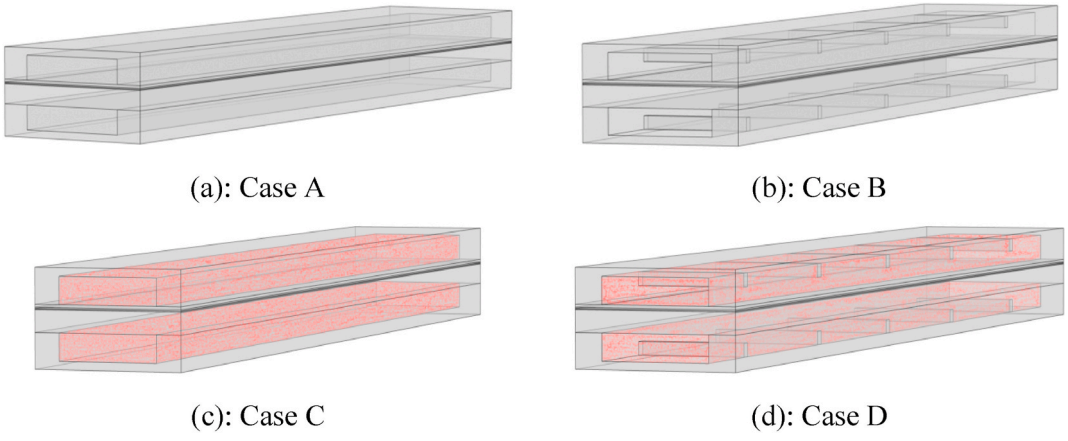

Fig. 2. Schematic of the SOFC for the 4 different flow field cases.

3.2. Velocity distribution

Fig. 5 displays the velocity field in the anode side and the cathode side for the four cases. The velocity in the air channel is higher than in the fuel channel in order to manage and deliver sufficient oxygen. As can be seen, the velocity is higher along the core zone of channels. Once fuel and air encounter the cell wall, the gases lose momentum, and the speed decreases. The velocity within the electrodes is also very low due to the small permeation employed in the simulation (k = 1.73e-11 m^2).

Fig. 5 shows the difference in velocities distributions at the medium surface of the gas channel (z = 50.5 mm). Comparing with the base case (case A), the application of obstacles in the case B causes an increase in velocities under the blocks. In addition, the metal foam used as a flow distributor (case C), creates a more uniform distribution of the velocity fields in the channel of the cell, the anodic and cathodic regions having almost the same velocity field values. In case D, the placement of obstacles in the presence of a metal foam, induces the same velocity flow distribution as in case B, but with greater values.

Fig. 6 illustrates a cross-sectional view of the velocity field at the half width section of the fuel cell (the half width section is defined as plane ABCD in Fig. 4b (for x = 1.5 mm)).

The upmost electrode flow velocity in a straight channel is lower than 2 m/s for the base case (Fig. 6 (case A)), whereas, it attains 4.38 m/s at the cathode channel and 3.33 m/s at the anode channel, by placing obstacles in the flow channels. It can be easily observed that the velocity is much higher in regions over the obstacles, forcing the reactant gases to flow into the electrodes: as a consequence, the mass flow rate of hydrogen and oxygen in the diffusion, support and active layers is enhanced (case B).

In addition to fostering a more uniform velocity distribution in the flow field as mentioned above, using a metal foam results in a smoother flow transport and an increase in velocity from 1.98 m/s to 2.59 m/s in the cathode flow channel, which significantly reinforces the mass transfer of gases throughout the electrode diffusion layers (case C).

The adoption of both metal foam and obstacles within the channels (case D) improves the uniformity of flow distribution and significantly boosts the fluid velocity, particularly in the regions between the electrodes and the obstacles, where the reactant species saturation is evident. At high velocities, the flow changes from the Darcy regime to the Forchheimer regime due to the significant inertial effect [32,83,84]. The maximum flow field velocity in the anode side reaches 3.59 m/s (Fig. 6 (case D)), besides, it attains 5.76 m/s in the cathode channel, which is almost 3 times as high as the conventional channel. Consequently, a significant increase in the diffusion of oxygen and hydrogen into the porous electrodes is facilitated.

3.3. Pressure drop

Fig. 7a and b presents the pressure drop along the centerline of the surface between channels and electrodes for all the cases (A, B, C and D). At the entrance of the SOFC, the pressure drop is quite elevated in response to the high velocity of the flows. The flow is propelled forward by the driving force of the pressure drop, which diminishes to a minimum value at the outlet.

As expected, the pressure drop in case D at the interface between the channels and electrodes is considerably higher compared to the other cases, both at the anode side (Fig. 7a) and the cathode side (Fig. 7b). Using a metal foam as a flow distributor alongside the placement of 5 obstacles results in a larger pressure drop compared with the base case A. Additionally, it is evident that the pressure drop increases locally where the obstacles are arranged, compelling the fluid to move towards the porous media.

Similarly, case B indicates a rise of pressure drop compared with base case A. Although the presence of obstacles in the channel enhances the mass transfer in active layers, their impact is much lower compared with the case C.

When metal foam is employed as a flow distributor in the channel flow (case C), the pressure drop is relatively high, compared with case A and case B. In this case, the pressure drop at the entrance of the channel is increased by 4 % in the anode side and by 62 % in the cathode side due to a frictional force between the flow and solid areas of the porous electrodes.

In general, it is also observed that the pressure drop in the cathode (Fig. 7b) is greater than the pressure drop in the anode (Fig. 7a), reaching about 2 times higher in case C and D. This occurs because the mass flow rate on the anode side is lower than that on cathode side.

3.4. Species transport

In order to perceive the hydrogen penetration flow within SOFC, Fig. 8 represents the profile of total quantity of fluid transported by convection and diffusion along the cell at the channel-anode support layer interface. As can be seen, the use of a metal foam enhances convection and diffusion fluxes, facilitating infiltration into the anode. The total flux reaches about 3×10^{-5} kg/m^2.s in case C, which is higher than the base case flux (2×10^{-5} kg/m^2.s) while following a similar trend along the cell. The presence of blocks (case B) induces pronounced peaks in hydrogen flux above them. The total flux in this case reaches 9×10^{-5} kg/m^2.s, whereas, it exceeds 10×10^{-5} kg/m^2.s in case D.

Figs. 9 and 10 present the hydrogen and water mass fraction distribution respectively of the x-z plane (2D) along the interface between anode and electrolyte (IAE) for different cases. It is worth noting that the color scale in these figures is maintained similar for convenient comparison.

In Fig. 9, It is obvious that the highest mass fraction is observed at the fuel inlet, and it reduces along the fuel channel direction, especially under the ribs of interconnects due to hydrogen consumption through electrochemical reaction.

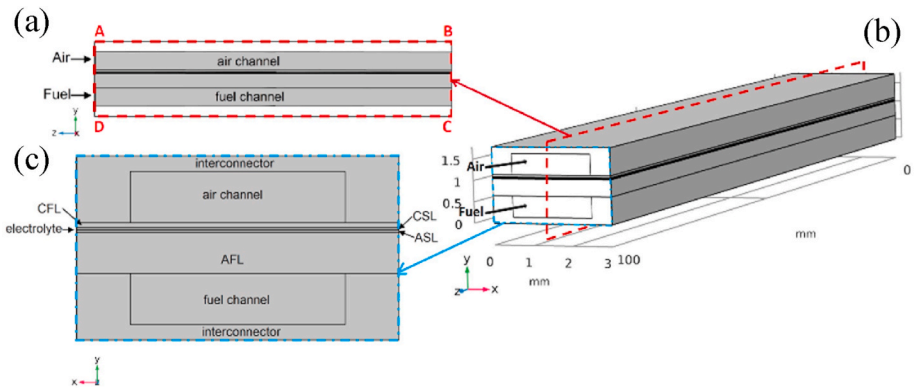

Fig. 4. (a) 3D computational domain of SOFC, (b) plane ABCD at the mid-width location of the cell (c) two-dimensional front view.

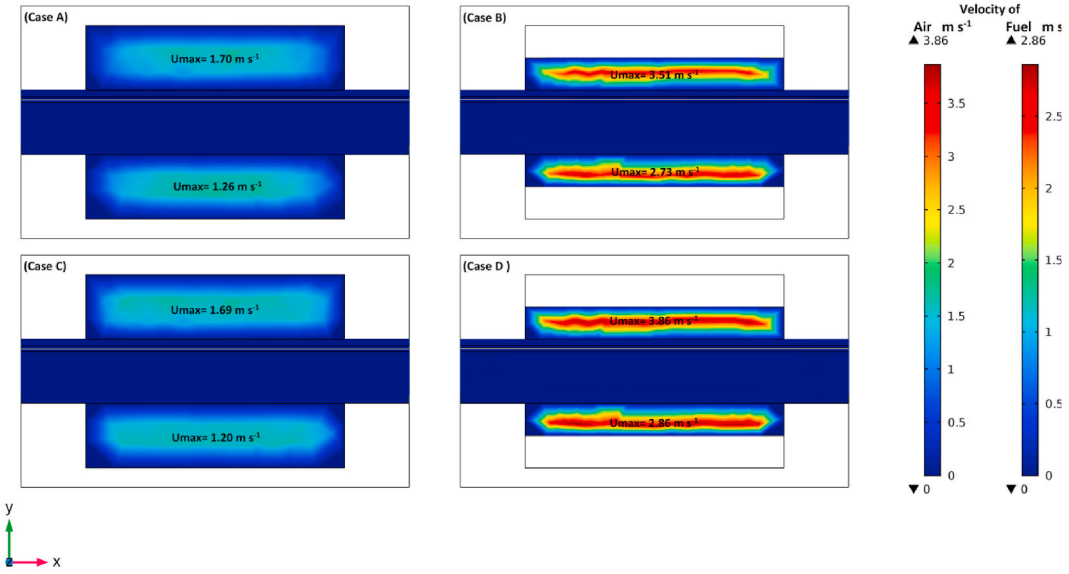

Fig. 5. The velocity distributions in the anode side and cathode side (z = 50.5 mm).

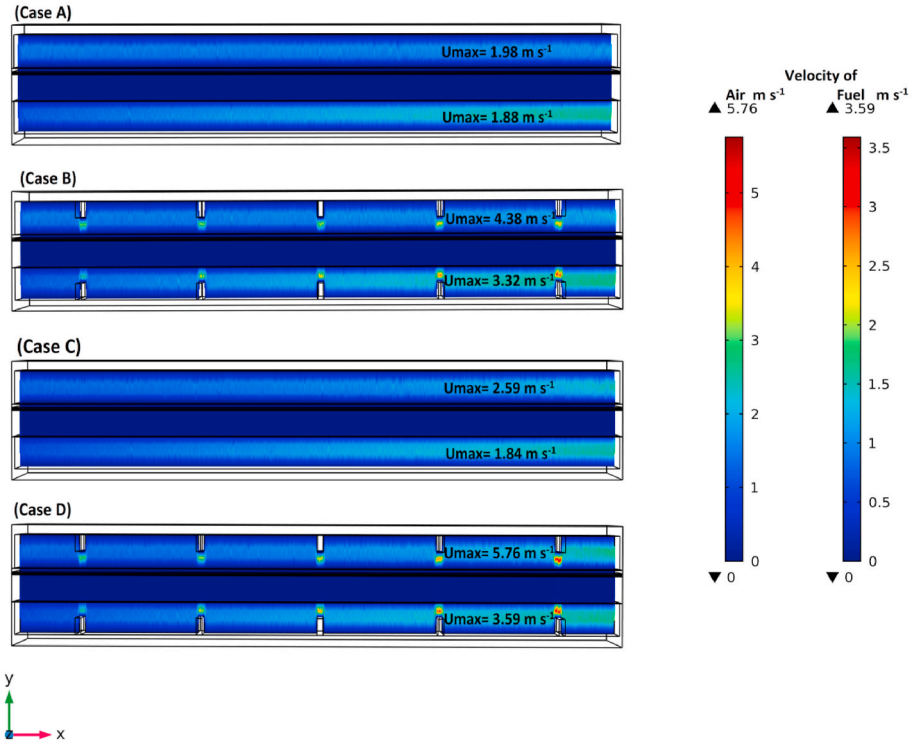

Fig. 6. Cross section of velocity distribution at the middle of SOFC (x = 1.5 mm).

In general, the mass fraction distribution of hydrogen in the cases B, C and D decreases compared with case A. It is evident that the use of a metal foam leads to a relatively higher consumption of hydrogen due to the uniform distribution and the elevated pressure drop, allowing the reactant gas to be introduced into the entire anode (cases C and D). Moreover, adding the obstacles could significantly increase the mass transfer throughout the catalyst layer, leading to an enhancement and enlargement of the mass fraction of hydrogen on the local surface where the obstacles are arranged (cases B and D).

Fig. 10 shows an enhanced water stream generation at the surface where the electrochemical reactions occur when metal foam and obstacles are present. The case D presents the highest water production rate compared to the base case A. The mass fraction is minimal at the inlet then it increases along the main flow direction, particularly under ribs where the electrochemical reactions predominantly take place.

The efficiency of the reaction is enhanced due to the sufficient penetration of reactive molecules into the porous electrode and their access to the reaction zone. As a result, more oxygen and hydrogen are consumed and consequently more water is produced.

The emergence of the peaks observed above the obstacles is a result of the large amount of water produced in this area. As a consequence, an improvement in current density output occurs.

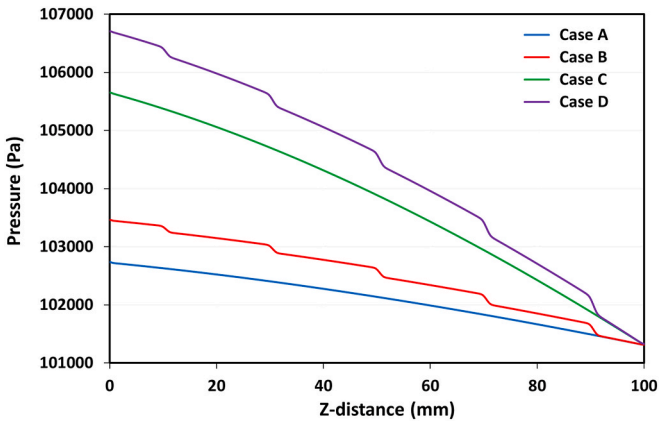

Fig. 7a. Pressure drop at the surface between channel and anode (x = 1.5 mm, y = 1.05 mm).

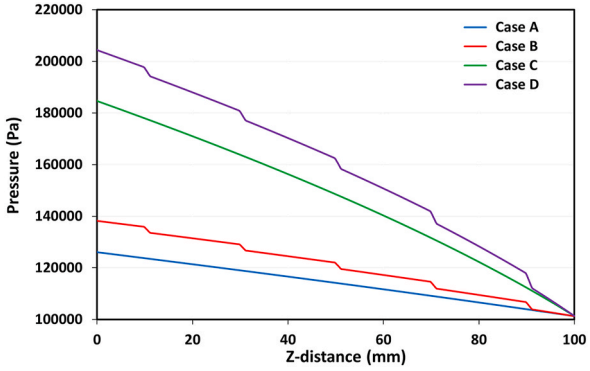

Fig. 7b. Pressure drop at the surface between channel and cathode (x = 1.5 mm, y = 1.145 mm).

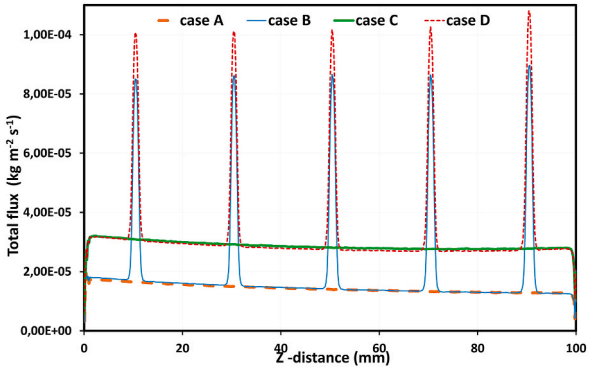

Fig. 8. The total flux of hydrogen at the interface channel flow-anode support layers (x = 1.5 mm, y = 0.65 mm).

3.5. Current distribution

The distribution of current density at the IAE interface on the anode side is represented in Fig. 11 for the four cases; note that the color scale is maintained similar for comparison. Generally, the current distribution profiles are approximately similar in all the cases. As illustrated, at the anode inlet where the concentration of fuel is most intense, the electronic current density seems higher, but reduces noticeably in the main flow direction as oxygen and hydrogen are consumed and the steam water and electrons are generated towards the outlet (z direction). In the direction normal to the main flow direction (x direction), the highest electrode current density is close to the channel/interconnect ribs interfaces. The concentration of oxygen in this region is high and the electron transfer distance is short. Moreover, the fuel concentration diminishes along the fuel flow direction, and reaches the minimal mole fraction at the outlet which induces the lowest current densities.

As depicted in this Figure, in case B the current density profile experiences five peaks and its maximum value I_{max} increases by 6.4 %, owing to the enhanced pressure drop and reactant concentration over the obstacles, compared to the base configuration (case A). However, the current density distribution is considerably more intense and uniform a using metal foam (case C) due to the significant reactants transfer volume, and I_{max} boosts by 26.4 %. As expected, the higher efficiency is noticed in case D, in which the maximum current density increases to 2040.9 A/m^2 compared to 1524.5 A/m^2 of the base channel, achieving an improvement of 33.9 %.

Fig. 12 displays the local current density at the middle plane of the electrolyte: as can be seen, the current density profiles follow a similar trend as pressure drop profiles.

For instance, in the cases without obstacles profiles exhibit a smooth trend, while in the other cases, they display peaks because of the higher reactant concentration in the areas directly over the obstructions. At the output of the channel, the current density decreases due to the reduced reactants concentration.

In this study, The Butler-Volmer equation [21] and the exchange current density [22,23], which are functions of partial pressure of gases, are used to determine the current density. By assuming the gases as ideal, their activities in electrodes depend on their partial pressures, which are affecting the exchange current density and consequently the cell current density.

3.6. Electrical performance

As plotted in Fig. 13, the polarization curves reveal that Case D presents superior performance compared with other cases. In general, in the low current density range (0–5000 A m^{-2}), there is a negligible difference between the four types of channels, then the selected zone in the figure demonstrates the disparity of polarization at V = 0.7 V; beyond this point, the obstacles and metal foam contribute to the slightly better performance, because mass transport losses predominate in the region with high current density.

3.7. Results comparison with prior research

From the wide literature, it has been proved that the flow field design has an important impact on the overall behavior of fuel cells. Numerous studies are being conducted to address the main problems, such as the mass transfer issues and the irregular distribution of reactants. In this regard, the flow field design is highly affecting the distribution and the transfer of species in the diffusion and catalyst layers of the electrodes, and consequently the performance of the fuel cell. Therefore, several design modifications are being developed, such as placing different shapes of obstacles throughout the channel and using metal foam as a flow distributor on the serpentine, parallel, or single flow field.

Table 5 provides an overview of various flow field designs and fuel cell operating parameters that have been examined experimentally and numerically, together with the main results obtained.

4. Discussion

A comprehensive comparison of four different types of channels is performed based on the distribution of velocity field, mass fraction of reactants, pressure drop and current density of the SOFC operating at the same operating conditions. Generally, the performance of the cell improves as more reactant gases (hydrogen and oxygen) are consumed, meaning that in areas where reactants are accessible, a higher local current density can be achieved due to increased electrochemical

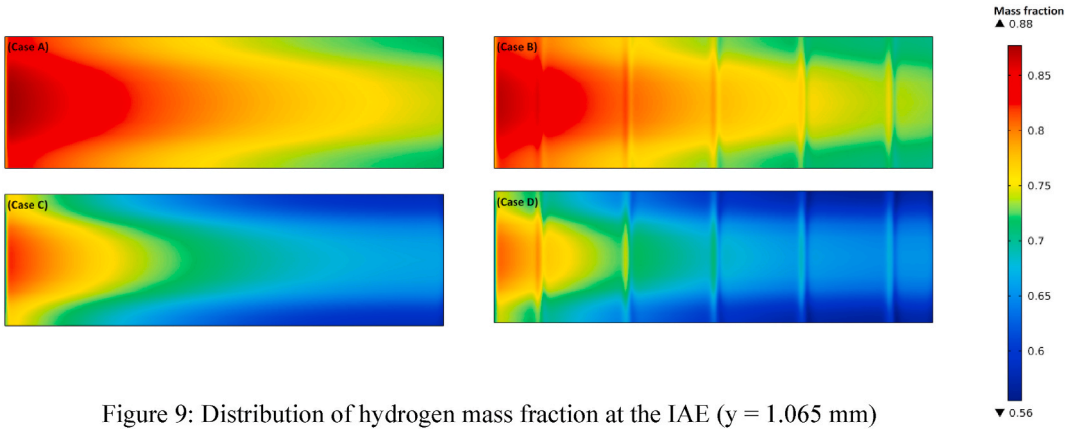

Figure 9: Distribution of hydrogen mass fraction at the IAE (y = 1.065 mm)

Fig. 9. Distribution of hydrogen mass fraction at the IAE (y = 1.065 mm).

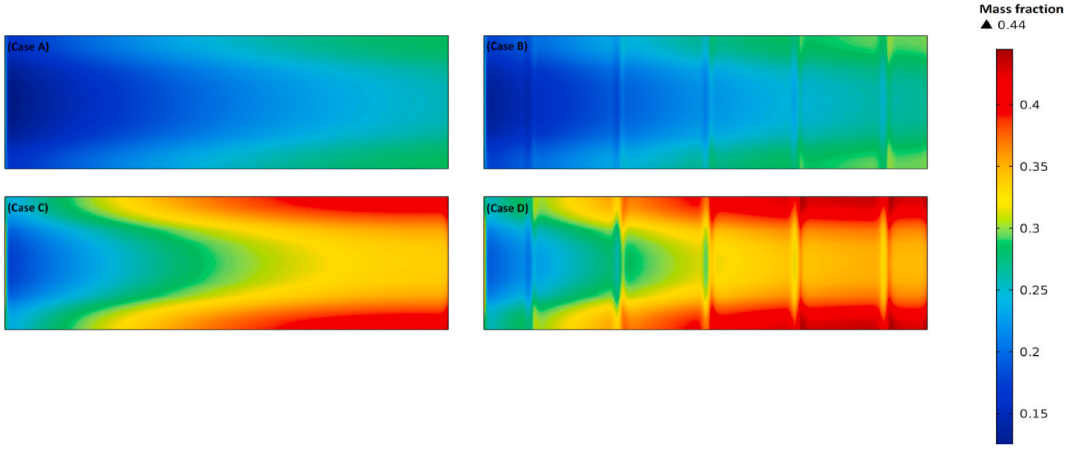

Fig. 10. Distribution of water mass fraction at the IAE (y = 1.065 mm).

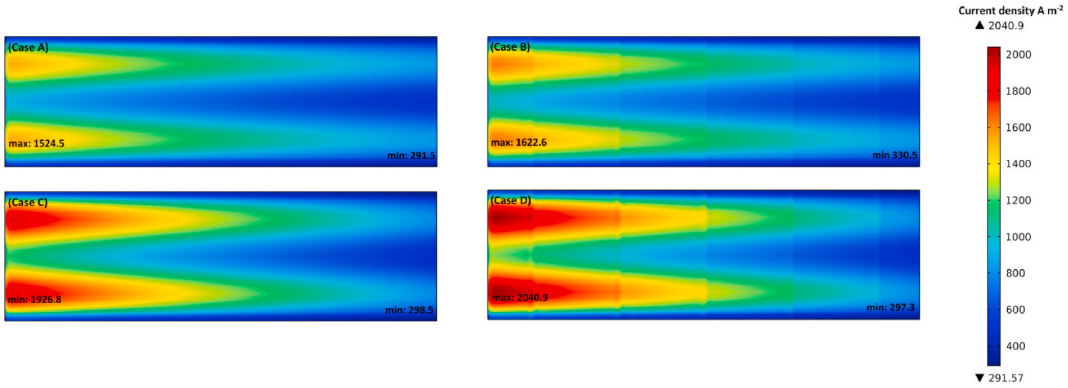

Fig. 11. Distribution of current density at the IAE (y = 1.065 mm).

reactions occurring, especially in the anode reaction layer.

Placing obstacles at regular intervals in the electrode channels restrains the flow area and leads to boost the pressure of gases mainly in regions over the obstacles; consequently, the flow field is accelerated and forced to deviate the direction towards the porous electrodes, allowing higher rate and deeper penetration of species up to the reaction layers, this resulting in an increase in the level of available fuel and oxidant and in an enhancement of electrochemical reactions. Although the positive effect of using obstacles, the current density is locally improved outstandingly mostly in the regions above these obstructions (Fig. 12 case B).

In present work, a metal foam that offers very unique mass transfer features is used as flow distributor as an alternative to conventional channels. The high porosity of the metal foam (≈90 %) and the spatial random pore structure allows convective gas flow throughout it with low flow resistance and more uniform distribution [42]. Nevertheless, the presence of rib features and the narrow channel where the foam is placed induces an increase in the pressure drop. This aspect is crucial to assess as it determines whether the flow can provide a sufficient driving force to transport any possible condensate produced through the fluid

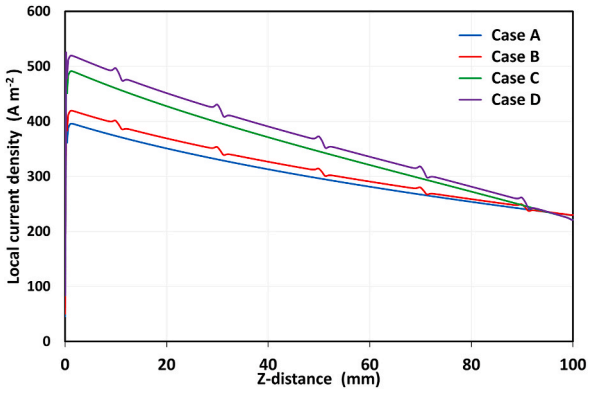

Fig. 12. Local current density at the middle plane of the electrolyte (x = 1.5 mm, y = 1.07 mm).

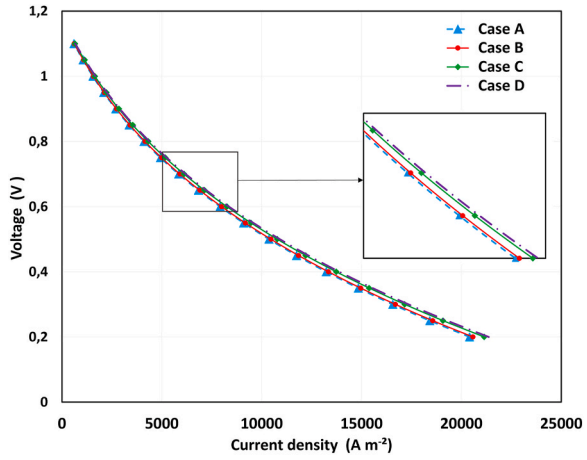

Fig. 13. Polarization curves for different cases.

flow structure [33]. In this porous media, the high pressure drop is attributed to the form drag, occurring due to a pressure difference across a boundary, as well as control over frictional drag in the metal foam [84, 85]. So that, it presents a suitable design for enhancing mass transfer to the catalyst layer and providing better uniformity in the concentration distribution of reactant species, leading to a much higher performance of current density.

Therefore, the adoption of both metal foam and obstacles inside the channels achieves the best performance of the SOFC by maximizing the species transport towards the reaction layers and optimizing the electrochemical reaction conditions. According to Fig. 11 (case D), it is clear that it has the highest current density value compared with other cases. Metal foam and obstacles, which are merged and considered as a new flow channel, lead to deliver the highest amount of fluid flow inside the electrode (Fig. 8) and cover a wider region, due to the reduced thickness and the flow redistribution through the height of cell. In other words, this configuration induces a volume flow decrease and internal pressure increase that results in turn in a higher cell potential own to the Nernst equation. Actually, the polarization curve that illustrates the performance of the SOFC varies depending on the design of the channel flow field. The internal flow modification has a significant effect on the polarization curves principally at low operating voltages given that mass transport losses are most prevalent in the area with high current density.

5. Conclusion

In the present study, metal foam and flow channel indentation are proposed to replace the conventional straight channels for the SOFCs. A three-dimensional model of a hydrogen-fueled single SOFC has been developed to compare four different cases: the basic SOFC with simple parallel flow channels (case A), with obstacles in the flow channels (case B), with metal foam as a flow distributor (case C), and with metal foam and obstacles simultaneously (case D).

Conservation equations of mass, species, momentum, energy and charge (electrons and ions) were used. The simulation involved fuel and air flow channels, electrode support, diffusion and active layers, electrolytes, and interconnects.

The model was validated over experimental data from the literature and employed to investigate the impacts of velocity, pressure and fuel mass fraction on the SOFC performance in the different cases.

The key results and conclusions can be summarized as follows.

- Placing obstacles in the flow channels (case B) led to an increase in velocity and pressure drop, mainly in regions over the obstacles. This forced the reactants to flow into the electrodes, thereby enhancing and enlarging the mass fraction of reactants on the local surface where the obstacles are arranged, consequently boosting the current density.
- Compared to cases A and B, using metal foam as a flow distributor (case C) significantly improved the performance of the SOFC. Reactant gases were more uniformly distributed and transferred in the gas active layer, resulting in increased consumption of hydrogen and production of water. The maximum current density increased by 26.4 % in this case.
- Adopting both metal foam and obstacles inside the channels resulted in the best performance for the SOFC, with a 34 % improvement in the maximum current density. The new flow channel design ensured uniform distribution of fuel and electrical conductivity, with a remarkable enhancement observed above the obstacles due to the combined effects of pressure drop and mass transfer in porous media.

Symbols

C_p Specific heat capacity [J kg^{-1}K^{-1})]	eff Effective
D_{ij} Molecular diffusivity [m^2 s^{-1}]	IAE Interface anode-electrolyte
d_j Driving force for diffusion [m^{-1}]	ref Reference
$D_{k,ij}$ Knudsen diffusivity of species [m^2 s^{-1}]	TPB Triple phase boundary
E Voltage [V]	SOFC Solid oxide fuel cell
F Faraday's constant [C mol^{-1}]	
i_0 Exchange current density [A m^{-2}]	*Greek symbols*
i_v Volumetric current density [A m^{-3}]	ε Porosity
j_i Mass flux [kg m^{-2} s^{-1}]	η Over potential [V]
M_i Molecular mass [kg mol^{-1}]	k Permeability tensor of the porous medium [m^2]
n_e Number of participating electrons	μ Dynamic viscosity [kg m^{-1} s^{-1})]
N_i Molar flux [mol m^{-2} s^{-1}]	ρ Density [kg m^{-3}]
P Pressure [Pa]	σ Charged-species conductivity [S m^{-1}]
Q_h Source term (heat) [W m^{-2}]	τ Tortuosity factor
Q_m Source term (mass) [kg m^{-3} s^{-1}]	φ Electric potential [V]
R Universal gas constant [J mol^{-1} K^{-1})]	ω_i Mass fraction
T Temperature [K]	
u Velocity [m s^{-1}]	
ν_i stoichiometric coefficient of components i	*Subscripts*
ΔS_r Entropy change [J mol^{-1} K^{-1})]	a Anode
	b Bulk
	c Cathode
Abbreviation	e Electrode
act Activation	el Electrolyte
AFL Anode active layer	i,j Specie index
ASL Anode support layer	l Ion transfer material
CDL Cathode diffusion layer	m Reaction m
CFL Cathode active layer	s Electron transfer material

CRediT authorship contribution statement

Asma Naouar: Writing – original draft, Validation, Software, Methodology, Investigation, Formal analysis, Data curation, Conceptualization. **Domenico Ferrero:** Writing – review & editing, Validation,

Table 5
A comparative overview of previous studies.

Authors	Type of fuel cell	Type of flow channel	Operating conditions	Type of study	Remarks
Heihdary. H et al. [29]	PEMFC	- Parallel flow field with partial/ full blockage (1–5 blocks)	1 bar/353.15 K	Numerical	- Net power is enhanced up to 30 % with more blocks number (5) and 100 % blockage in the cathode
Kuo. J.K et al. [30]	PEMFC	- Wavy channel	1 bar/323-333-343 K	Numerical	- The wave form channel generates better catalytic transfer, convective heat transfer and power density
Tiss. F et al. [31]	PEMFC	- Single channel with 4 partial blocks	1 bar/300 K	Experimental and numerical	- Titl angle of partial blocks has an impact on the cell performance, it improves in the presence of blocks
Wan. Z et al. [32]	PEMFC	- M-flow channel	101.3 kPa/343 K	Numerical	- M-flow channel produces 21.3 % power density better than the wave flow channel
Chellehbari Y.M et al. [33]	SOFC	- Conventional channel with (3-7) rectangle, trapezoidal and triangular obstacles	1 bar/1073.15 K	Numerical	- Overpotential decreases as the number of obstacles increases. - Fuel Cell power enhances using obstacles and reaches 35 % with 7 triangular obstacles.
Bilgili. M et al. [34]	PEMFC	- Single channel – 49 cases (porous/baffled channel)	202.65 kPa/328.15 K	Numerical	- Different cases affect water saturation and temperature. - Baffled flow field without biporous layers is the best performing case.
Dehsara. M et al. [36]	PEMFC	- Flat channel bed - semicircular channel bed - wavy channel bed	1 bar/353 K	Numerical	- channel indentation improves the cell performance up to 22 %.
Cai. G et al. [37]	PEMFC	- Bio- inspired wavy channel	101.3 kPa/343.15 K	Numerical	- Power density was improved by 22 % due to reduced resistance to reactant flow.
Ghanbarian. A et al. [38]	PEMFC	- Parallel flow field with trapezoidal, semi-circular and square dents.	100 kPa/333 K	Numerical	- Trapezoidal dent displays the best performance.
Perng. S et al. [39]	HT-PEMFC	- Bipolar-plate channel with bottomed baffles (1–7)	1 bar/453 K	Experimental and numerical	- Five bottomed-baffle channel has the best impedance and 8 % of power improvement.
Tseng. C.J et al. [42]	PEMFC	- Flow channel plate and metal foam as flow distributor	1 bar/ 303.15–353.15 K	Experimental	- Metal foam has a light weight and a unique mass transport property (reactant gases move with less flow resistance).
Afshari. E et al. [43]	PEMFC	- flow channel plate and metal foam as flow distributor	151.987 kPa/ 303.15 K (dry side) 353.15 K (wet side)	Numerical	- Membrane humidifier containing metal foam has higher efficiency.
Vazifeshenas. Y et al. [44]	PEMFC	- Serpentine, parallel and multichannel flow field with metal foam	1 bar/283 K	Numerical	- Raising metal foam porosity reduces pressure drop and the transfer of heat.
Park.J.E et al. [45]	PEMFC	- Serpentine flow field - Foam flow field (with metal foam)	1 bar/243.15 K	Experimental	- Foam flow field enhances electrochemical reaction of the catalyst layer and increases cell performance.
Hossain.M.S et al. [46]	PEMFC	- Parallel channel cathode flow field with metal foam.	0.5 bar (inlet)/ ~313.15 K	Experimental	- Metal foam enhances temperature distribution and diffusion of gas to electrodes. - Water removal is observed.
Kumar. A et al. [48,50,51]	PEMFC	- Channel flow field with metal foam.	101.3 kPa 353 K	Numerical	- Average current density increases as permeability of metal foam decreases. - Metal foam ensures more uniform distribution of current density and better performance. - Permeability of the metal foam has a considerable impact on fuel cell efficiency.
Afshari. E et al. [49]	PEMFC	- Parallel flow field with partial restricted cathode channel and metal foam as channel.	101.3 kPa/353 K	Numerical	- Oxygen concentration and Current density were raised by the inclusion of baffle plate and metal foam
Toghyani. S et al. [52]	PEMFC	- Serpentine and parallel flow field with metal foam as flow distributor.	1.5 bar/353 K	Numerical	- A proper metal foam permeability should be chosen for optimum pressure.
Tsai. B.T et al. [53]	PEMFC	- Bipolar plate with metal foam as flow distributor.	1 bar/323.15 K	Experimental	- Metal foam improves the uniformity of gas reactant distribution in the catalyst layer.
Gondolini. A et al. [54]	MS-SOFC	–	~373.15 K	Experimental	- Use NiCrAl metal foam as metal support for SOFC application
Zeilke.P et al. [56]	SOC SOEC SOFC	–	973.15 K	Experimental	- Using CuMn foam as a cathode contact material increase the level of serial resistance during constant operation of the fuel cell.
Iwai. H et al. [57]	SOFC	- Single plate	882.15 K	Numerical	- Porous material as flow distributor ensures current collected and more uniform distribution flow.
Zhan. R et al. [58]	SOFC	- Straight channel and metal foam as cathode flow distributor.	1 bar/1073 K	Numerical	- metal foam as a cathode flow field distributor lead to an enhancement of the output power by 13.74 % compared with conventional channel oxygen concentration, electron transport and temperature of SOFC are uniformly distributed.
Present work	SOFC	- Single channel flow field with 5 obstacles and metal foam as flow distributor.	1 bar/1000 K	Numerical	- Placing obstacles induces velocity and pressure drop increment, and enhances mass transfer to active layers, the maximum current density increases by 6.4 %. - Using a metal foam as a flow distributor provokes a uniform distribution of reactant gases, the maximum current density rises by 26 %. - Adopting both metal foam and obstacles inside the channels, the SOFC achieves the best performance with a 34 % improvement in the maximum current density due to uniform distribution of fuels and electrical conductivity.

Supervision, Software, Methodology, Investigation, Formal analysis, Conceptualization. **Massimo Santarelli:** Writing – review & editing, Validation, Supervision, Software, Methodology, Investigation, Formal analysis, Conceptualization. **Hacen Dhahri:** Writing – review & editing, Supervision, Investigation, Conceptualization. **Abdallah Mhimid:** Writing – review & editing, Supervision, Investigation, Conceptualization.

Declaration of competing interest

The authors declare that they have no known competing financial interests or personal relationships that could have appeared to influence the work reported in this paper.

Acknowledgments

This publication is part of the project NODES which has received funding from the MUR – M4C2 1.5 of PNRR funded by the European Union - NextGenerationEU (Grant agreement no. ECS00000036).

References

[1] J.B. Young, Thermofluid modeling of fuel cells, Annu. Rev. Fluid Mech. 39 (2007) 193–215.
[2] S. Mekhilef, R. Saidur, A. Safari, Comparative study of different fuel cell technologies, Renew. Sustain. Energy Rev. 16 (1) (2012) 981–989.
[3] O.Z. Sharaf, M.F. Orhan, An overview of fuel cell technology: fundamentals and applications, Renew. Sustain. Energy Rev. 32 (2014) 810–853.
[4] M. Zunita, A. Raizki, R. Aditya, I.G. Wenten, Proton exchange polyionic liquid-based membrane fuel cell applications, Results in Engineering 16 (2022) 100653.
[5] Y. Yang, Z. Wu, R. Li, H. Wang, J. Ren, B. Li, Z. Zhang, Review on the thermal neutrality of application-oriented liquid organic hydrogen carrier for hydrogen energy storage and delivery, Results in Engineering 19 (2023) 101394.
[6] A.L. Dicks, Hydrogen generation from natural gas for the fuel cell systems of tomorrow, J. Power Sources 61 (1e2) (1996) 113e24.
[7] S. Park, J.M. Vohs, R.J. Gorte, Direct oxidation of hydrocarbons in a solid-oxide fuel cell, Nature 404 (2000) 265e7.
[8] R.J. Gorte, S. Park, J.M. Vohs, C.H. Wang, Anodes for direct oxidation of dry hydrocarbons in a solid-oxide fuel cell, Adv. Mater. 12 (2000) 1465e9.
[9] P. Aguiar, C.S. Adjiman, N.P. Brandon, Anode-supported intermediate temperature direct internal reforming solid oxide fuel cell. I: model-based steady-state performance, J. Power Sources 138 (2004) 120e36.
[10] C. Sun, U. Stimming, Recent anode advances in solid oxide fuel cells, J. Power Sources 171 (2007) 247e60.
[11] A.F. Al-Attar, H.A. Jaber, R.A. Anaee, Produce solid oxide fuel cell anodes as (BaTiO3) 100− x−(MgO) x for clean energy, Results in Engineering 19 (2023) 101327.
[12] M. Aravindan, P. Kumar, Hydrogen towards sustainable transition: a review of production, economic, environmental impact and scaling factors, Results in Engineering (2023) 101456.
[13] M. Sadeghi, M. Jafari, Y.S. Hajimolana, T. Woudstra, P.V. Aravind, Size and exergy assessment of solid oxide fuel cell-based H2-fed power generation system with alternative electrolytes: a comparative study, Energy Convers. Manag. 228 (2021) 113681.
[14] O. Corigliano, P. Fragiacomo, Extensive analysis of SOFC fed by direct syngas at different anodic compositions by using two numerical approaches, Energy Convers. Manag. 209 (2020) 112664.
[15] Z. Yan, A. He, S. Hara, N. Shikazono, Modeling of solid oxide fuel cell (SOFC) electrodes from fabrication to operation: correlations between microstructures and electrochemical performances, Energy Convers. Manag. 190 (2019) 1–13.
[16] R. Zhang, J. Cao, W. Wang, E. Tan, R. Zhu, W. Chen, Y. Zhang, Research on design strategies and sensing applications of energy storage system based on renewable methanol fuel, Results in Engineering 20 (2023) 101439.
[17] M. Saied, K. Ahmed, M. Nemat-Alla, M. Ahmed, M. El-Sebaie, Performance study of solid oxide fuel cell with various flow field designs: numerical study, Int. J. Hydrogen Energy 43 (45) (2018) 20931–20946.
[18] D. Bhattacharya, J. Mukhopadhyay, N. Biswas, R.N. Basu, P.K. Das, Performance evaluation of different bipolar plate designs of 3D planar anode-supported SOFCs, Int. J. Heat Mass Tran. 123 (2018) 382–396.
[19] J.D. Duhn, A.D. Jensen, S. Wedel, C. Wix, Optimization of a new flow design for solid oxide cells using computational fluid dynamics modelling, J. Power Sources 336 (2016) 261–271.
[20] Z. Qu, P.V. Aravind, S.Z. Boksteen, N.J.J. Dekker, A.H.H. Janssen, N. Woudstra, A. H.M. Verkooijen, Three-dimensional computational fluid dynamics modeling of anode-supported planar SOFC, Int. J. Hydrogen Energy 36 (16) (2011) 10209–10220.
[21] V.A. Danilov, M.O. Tade, A CFD-based model of a planar SOFC for anode flow field design, Int. J. Hydrogen Energy 34 (21) (2009) 8998e9006.
[22] J. Moreno-Blanco, F. Elizalde-Blancas, J.M. Riesco-Avila, J.M. Belman-Flores, A. Gallegos-Muñoz, On the effect of gas channels-electrode interface area on SOFCs performance, Int. J. Hydrogen Energy 44 (1) (2019) 446–456, 2019.
[23] R.M. Manglik, Y.N. Magar, Heat and mass transfer in planar anode-supported solid oxide fuel cells: effects of interconnect fuel/oxidant channel flow cross section, J. Therm. Sci. Eng. Appl. 7 (4) (2015) 041003.
[24] I. Khazaee, A. Rava, Numerical simulation of the performance of solid oxide fuel cell with different flow channel geometries, Energy 119 (2017).
[25] C. Huang, S. Shy, C. Lee, On flow uniformity in various interconnects and its influence to cell performance of planar SOFC, J. Power Sources 183 (2008) 205e13.
[26] Z. Lin, J.W. Stevenson, M.A. Khaleel, The effect of interconnect rib size on the fuel cell concentration polarization in planar SOFCs, J. Power Sources 117 (1–2) (2003) 92–97.
[27] I. Khazaee, Effect of placing different obstacles in flow fields on performance of a PEM fuel cell: numerical investigation and experimental comparison, Heat Mass Transf. und Stoffuebertragung 49 (9) (2013) 1287–1298.
[28] H.W. Wu, D.Y. Kang, S.W. Perng, Effect of rectangular ribs in the flow channels of HTPEM Fuel Cell by a three-dimensional model, Energy Proc. 105 (2017) 1376–1381.
[29] H. Heidary, M.J. Kermani, B. Dabir, Influences of bipolar plate channel blockages on PEM fuel cell performances, Energy Convers. Manag. 124 (2016) 51–60.
[30] J.K. Kuo, T.H. Yen, C.K. Chen, Three-dimensional numerical analysis of PEM fuel cells with straight and wave-like gas flow fields channels, J. Power Sources 177 (1) (2008) 96–103.
[31] F. Tiss, R. Chouikh, A. Guizani, A numerical investigation of reactant transport in a PEM fuel cell with partially blocked gas channels, Energy Convers. Manag. 80 (2014) 32–38.
[32] Z. Wan, W. Quan, C. Yang, H. Yan, X. Chen, T. Huang, S. Chan, Optimal design of a novel M-like channel in bipolar plates of proton exchange membrane fuel cell based on minimum entropy generation, Energy Convers. Manag. 205 (2020) 112386.
[33] Y.M. Chellehbari, K. Adavi, J.S. Amin, S. Zendehboudi, A numerical simulation to effectively assess impacts of flow channels characteristics on solid oxide fuel cell performance, Energy Convers. Manag. 244 (2021) 114280.
[34] M. Bilgili, M. Bosomoiu, G. Tsotridis, Gas flow field with obstacles for PEM fuel cells at different operating conditions, Int. J. Hydrogen Energy 40 (5) (2015) 2303–2311.
[35] L. Mihanović, Ž. Penga, L. Xing, V. Hacker, Combining baffles and secondary porous layers for performance enhancement of proton exchange membrane fuel cells, Energies 14 (12) (2021) 3675.
[36] M. Dehsara, M.J. Kermani, Proton exchange membrane fuel cells performance enhancement using bipolar channel indentation, J. Mech. Sci. Technol. 28 (1) (2014) 365∼376.
[37] G. Cai, Y. Liang, Z. Liu, W. Liu, Design and optimization of bio-inspired wave-like channel for a PEM fuel cell applying genetic algorithm, Energy 192 (2020) 116670.
[38] A. Ghanbarian, M.J. Kermani, Enhancement of PEM fuel cell performance by flow channel indentation, Energy Convers. Manag. 110 (2016) 356–366.
[39] S.W. Perng, H.W. Wu, Y.B. Chen, Y.K. Zeng, Performance enhancement of a high temperature proton exchange membrane fuel cell by bottomed-baffles in bipolar-plate channels, Appl. Energy 255 (2019) 113815.
[40] W. Yuan, Y. Tang, X. Yang, Z. Wan, Porous metal materials for polymer electrolyte membrane fuel cells–A review, Appl. Energy 94 (2012) 309–329.
[41] M.S. Hossain, B. Shabani, Metal foams application to enhance cooling of open cathode polymer electrolyte membrane fuel cells, J. Power Sources 295 (2015) 275–291.
[42] C.J. Tseng, B.T. Tsai, Z.S. Liu, T.C. Cheng, W.C. Chang, S.K. Lo, A PEM fuel cell with metal foam as flow distributor, Energy Convers. Manag. 62 (2012) 14–21.
[43] E. Afshari, N.B. Houreh, Performance analysis of a membrane humidifier containing porous metal foam as flow distributor in a PEM fuel cell system, Energy Convers. Manag. 88 (2014) 612–621.
[44] Y. Vazifeshenas, K. Sedighi, M. Shakeri, Heat transfer in PEM cooling flow field with high porosity metal foam insert, Appl. Therm. Eng. 147 (2019) 81–89.
[45] J.E. Park, W. Hwang, M.S. Lim, S. Kim, C.Y. Ahn, O.H. Kim, Y.E. Sung, Achieving breakthrough performance caused by optimized metal foam flow field in fuel cells, Int. J. Hydrogen Energy 44 (39) (2019) 22074–22084.
[46] M.S. Hossain, B. Shabani, Reticulated porous and parallel channel cathode flow fields in real scale polymer electrolyte membrane fuel cells: a comparative experimental study, Int. J. Hydrogen Energy 44 (47) (2019) 25905–25917.
[47] A. Fly, Q. Meyer, M. Whiteley, F. Iacoviello, T. Neville, P.R. Shearing, R. Chen, X-ray tomography and modelling study on the mechanical behaviour and performance of metal foam flow-fields for polymer electrolyte fuel cells, Int. J. Hydrogen Energy 44 (14) (2019) 7583–7595.
[48] A. Kumar, R.G. Reddy, Modeling of polymer electrolyte membrane fuel cell with metal foam in the flow-field of the bipolar/end plates, J. Power Sources 114 (1) (2003) 54e62.
[49] E. Afshari, M. Mosharaf-Dehkordi, H. Rajabian, An investigation of the PEM fuel cells performance with partially restricted cathode flow channels and metal foam as a flow distributor, Energy 118 (2017) 705e15.
[50] A. Kumar, R.G. Reddy, Materials and design development for bipolar/end plates in fuel cells, J. Power Sources 129 (1) (2004) 62e7.
[51] A. Kumar, R.G. Reddy, Polymer electrolyte membrane fuel cell with metal foam in the gas flow-field of bipolar/end plates, J New Mater Electrochem Syst 6 (4) (2003) 231e6.

[52] S. Toghyani, E. Afshari, E. Baniasadi, Metal foams as flow distributors in comparison with serpentine and parallel flow fields in proton exchange membrane electrolyzer cells, Electrochim. Acta 290 (2018) 506–519.
[53] B.T. Tsai, C.J. Tseng, Z.S. Liu, C.H. Wang, C.I. Lee, C.C. Yang, S.K. Lo, Effects of flow field design on the performance of a PEM fuel cell with metal foam as the flow distributor, Int. J. Hydrogen Energy 37 (17) (2012) 13060e6.
[54] A. Gondolini, E. Mercadelli, A. Sangiorgi, A. Sanson, Integration of Ni-GDC layer on a NiCrAl metal foam for SOFC application, J. Eur. Ceram. 37 (3) (2017) 1023–1030.
[55] P.A.N.G. Qiu, G.H. Wu, D.L. Sun, Z.Y. Xiu, Q. Zhang, Z.L. Hu, Compressive property and energy absorption characteristic of 3D open-cell NieCreFe alloy foams under quasi-static conditions, Trans. Nonferrous Metals Soc. China 22 (2012) s566e72.
[56] P. Zielke, A.C. Wulff, X. Sun, S.H. Jensen, R. Kiebach, H.L. Frandsen, A. Hagen, Investigation of a spinelforming Cu-Mn foam as an oxygen electrode contact material in a solid oxide cell single repeating unit, Fuel Cell. 17 (5) (2017).
[57] H. Iwai, Y. Yamamoto, M. Saito, H. Yoshida, Numerical simulation of intermediate-temperature direct-internal-reforming planar solid oxide fuel cell, Energy 36 (4) (2011) 2225e34.
[58] R. Zhan, Y. Wang, M. Ni, G. Zhang, Q. Du, K. Jiao, Three-dimensional simulation of solid oxide fuel cell with metal foam as cathode flow distributor, Int. J. Hydrogen Energy 45 (11) (2020) 6897–6911.
[59] T. Taner, The novel and innovative design with using H2 fuel of PEM fuel cell: efficiency of thermodynamic analyze, Fuel 302 (2021) 121109.
[60] T. Taner, Energy and exergy analyze of PEM fuel cell: a case study of modeling and simulations, Energy 143 (2018) 284–294.
[61] T. Taner, The micro-scale modeling by experimental study in PEM fuel cell, J. Therm. Eng. 3 (2017).
[62] M. Canavar, A. Mat, S. Celik, B. Timurkutluk, Y. Kaplan, Investigation of temperature distribution and performance of SOFC short stack with/without machined gas channels, Int. J. Hydrogen Energy 41 (2016) 10030–10036.
[63] C.M. Huang, S.S. Shy, C.H. Lee, On flow uniformity in various interconnects and its influence to cell performance of planar SOFC, J. Power Sources 183 (2008) 205–213.
[64] T. Dey, P.C. Ghosh, D. Singdeo, M. Bose, R.N. Basu, Diagnosis of scale up issues associated with planar solid oxide fuel cells, Int. J. Hydrogen Energy 36 (2011) 9967–9976.
[65] R. Scataglini, M. Wei, A. Mayyas, S.H. Chan, T. Lipman, M. Santarelli, A direct manufacturing cost model for solid-oxide fuel cell stacks, Fuel Cell. 17 (2017) 825–842.
[66] S. Harboe, A. Schreiber, N. Margaritis, L. Blum, O. Guillon, N.H. Menzler, Manufacturing cost model for planar 5 kWel SOFC stacks at Forschungszentrum Jülich, Int. J. Hydrogen Energy 45 (2020) 8015–8030.
[67] D. Ferrero, M. Gamba, A. Lanzini, M. Santarelli, Power-to-Gas hydrogen: techno-economic assessment of processes towards a multi-purpose energy carrier, Energy Proc. 101 (2016) 50–57.
[68] S.A.H. Naqvi, T. Taner, M. Ozkaymak, H.M. Ali, Hydrogen production through alkaline electrolyzers: a techno-economic and enviro-economic analysis, Chem. Eng. Technol. 46 (2023) 474–481.
[69] T. Taner, S.A.H. Naqvi, M. Ozkaymak, Techno-economic analysis of a more efficient hydrogen generation system prototype: a case study of PEM electrolyzer with Cr-C coated SS304 bipolar plates, Fuel Cell. 19 (2019) 19–26.
[70] M. Naeini, J.S. Cotton, T.A. Adams, An eco-technoeconomic analysis of hydrogen production using solid oxide electrolysis cells that accounts for long-term degradation, Front. Energy Res. 10 (2022).
[71] P. Marocco, M. Gandiglio, M. Santarelli, When SOFC-based cogeneration systems become convenient? A cost-optimal analysis, Energy Rep. 8 (2022) 8709–8721.
[72] X. Zhang, M. Espinoza, T. Li, M. Andersson, Parametric study for electrode microstructure influence on SOFC performance, Int. J. Hydrogen Energy 46 (2021) 37440–37459.
[73] X. Zhang, J. Parbey, G. Yu, T. Li, M. Andersson, Thermal stress analysis of solid oxide fuel cells with chromium poisoning cathodes, J. Electrochem. Soc. 165 (2018) F1224–F1231.
[74] Modeling with electrochemistry, COMSOL Multiphysics Version 5.5, Batteries and Fuel Cells Module Users Guide, chapter 2: modeling with electrochemistry, Stockholm, Sweden, 2019.
[75] Y. Patcharavorachot, A. Arpornwichanop, A. Chuachuensuk, Electrochemical study of a planar solid oxide fuel cell: role of support structures, J. Power Sources 177 (2008) 254–261.
[76] M. Andersson, SOFC Modeling Considering Mass and Heat Transfer, Fluid Flow with Internal Reforming Reactions, Licentiate Thesis, Lund University, Sweden, 2009.
[77] D. Ferrero, A. Lanzini, M. Santarelli, Solid oxide fuel cells modeling, in: M. Boaro, A. Salvatore (Eds.), Advances in Medium and High Temperature Solid Oxide Fuel Cell Technology, CISM International Centre for Mechanical Sciences, vol 574, Springer, Cham, 2017, pp. 291–342, 574.
[78] M. Andersson, J. Yuan, B. Sundén, SOFC modeling considering electrochemical reactions at the active three phase boundaries, Int. J. Heat Mass Tran. 55 (2012) 773–788.
[79] J. Shi, X. Xue, CFD analysis of a novel symmetrical planar SOFC design with micro-flow channels, J. Chem. Eng. 163 (2010) 119–125.
[80] A.V. Akkaya, Electrochemical model for performance analysis of a tubular SOFC, Int. J. Energy Res. 31 (2007) 79–98.
[81] M. Andersson, J. Yuan, B. Sunden, SOFC modeling considering hydrogen and carbon monoxide as electrochemical reactants, J. Power Sources 232 (2013) 42–54.
[82] Q. Fu, Z. Li, W. Wei, F. Liu, X. Xu, Z. Liu, Performance of a beam and slot interconnector for anode-supported SOFC stack, Energy Convers. Manag. 241 (2021) 114277.
[83] C. Lv, W. Li, J. Du, J. Liang, H. Yang, Y. Zhu, B. Ma, Experimental investigation of permeability and Darcy-Forchheimer flow transition in metal foam with high pore density, Exp. Therm. Fluid Sci. 154 (2024) 111149.
[84] P. Du Plessis, A. Montillet, J. Comiti, J. Legrand, Pressure drop prediction for flow through high porosity metallic foams, Chem. Eng. Sci. 49 (21) (1994) 3545–3553.
[85] N. Dukhan, Correlations for the pressure drop for flow through metal foam, Exp. Fluid 41 (2006) 665–672.